

# Dual-color co-filamentation in Argon

Pierre Béjot<sup>1,\*</sup>, Jérôme Kasparian<sup>1,2</sup>, Jean-Pierre Wolf<sup>1</sup>

(1) *Université de Genève, GAP-Biophotonics, 20 rue de l'Ecole de Médecine, 1211 Geneva 4, Switzerland*

(2) *Université Lyon 1; CNRS; LASIM UMR 5579, bât. A. Kastler, 43 Bd du 11 novembre 1918, F-69622 Villeurbanne Cedex, France*

[pierre.bejot@physics.unige.ch](mailto:pierre.bejot@physics.unige.ch)

**Abstract:** We investigate both experimentally and theoretically the mechanisms driving the co-filamentation of two ultrashort laser pulses at 800 and 400 nm in Argon. The cross-Kerr lens and cross-phase modulation between the two filaments of different colors bridging both the continuum spectra and the plasma channels induced by the individual pulses. This dual-color filamentation also results in the simultaneous generation of two few-cycle pulses at both 800 and 400 nm, providing a potential way to generate attosecond pulses.

© 2008 Optical Society of America

**OCIS codes:** (190.7110) Ultrafast nonlinear optics; (320.6629) Supercontinuum generation; (260.3230) Ionization; (320.5520) Pulse compression; (190.5940) Self-action effects; (260.5950) Self-focusing

---

## References and links

1. T. Pfeifer, M. Gallmann, M.J. Abel, D.M Neumark, and S.R Leone. Single attosecond pulse generation in the multicycle-driver regime by adding a weak second-harmonic field. *Opt. Lett.* **31**, 975-977, (2006).
2. M. Hentschel, R. Kienberger, Ch. Spielmann, G. A. Reider, N. Milosevic, T. Brabec, P. Corkum, U. Heinzmann, M. Drescher, and F. Krausz. Attosecond metrology. *Nature (London)* **414**, 509-513, (2001).
3. H.S. Chakraborty, M.B. Gaarde, and A. Couairon. Single attosecond pulses from high harmonics driven by self-compressed filaments. *Opt. Lett.* **31**, 3662-3664, (2006).
4. T. Brixner, N. H. Damrauer, P. Niklaus, and G. Gerber. Photosensitive adaptive femtosecond quantum control in the liquid phase. *Nature (London)* **414**, 57-60, (2001).
5. J. Kasparian, M. Rodriguez, G. Mejean, J. Yu, E. Salmon, H. Wille, R. Bourayou, S. Frey, Y. B. Andre, A. Mysyrowicz, R. Sauerbrey, J. P. Wolf, and L. Woste. White-light filaments for atmospheric analysis. *Science* **301**, 61-64, (2003).
6. A. Couairon and A. Mysyrowicz. Femtosecond filamentation in transparent media. *Phys. Rep.* **44**, 47-189, (2007).
7. L. Bergé, S. Skupin, R. Nuter, J. Kasparian, and J.-P. Wolf. Ultrashort filaments of light in weakly ionized, optically transparent media. *Rep. Prog. Phys.* **70**, 1633-1713, (2007).
8. J. Kasparian and J.-P. Wolf. Physics and applications of atmospheric nonlinear optics and filamentation. *Opt. Express* **16**, 466-493, (2008).
9. T. Fuji, T. Horio, and T. Suzuki. Generation of 12 fs deep-ultraviolet pulses by four-wave mixing through filamentation in neon gas. *Opt. Lett.* **32**, 2481-2483, (2007).
10. A. Zair, A. Guandalini, F. Schapper, M. Holler, J. Biegert, L. Gallmann, A. Couairon, M. Franco, A. Mysyrowicz, and U. Keller. Spatio-temporal characterization of few-cycle pulses obtained by filamentation. *Opt. Express* **15**, 5394-5404, (2007).
11. S.A Trushin, K. Kosma, W. Fuss, and E. Schmid. Sub-10-fs supercontinuum radiation generated by filamentation of few-cycle 800 nm pulses in argon. *Opt. Lett.* **32**, 2432-2434, (2007).
12. X. Chen, X. Li, J. Liu, P. Wei, X. Ge, R. Li, and Z. Xu. Generation of 5 fs, 0.7 mJ pulses at 1 KHz through cascade filamentation. *Opt. Lett.* **32**, 2402-2404, (2007).
13. T. Fuji and T. Suzuki. Generation of sub-two-cycle mid-infrared pulses by four-wave mixing through filamentation in air. *Opt. Lett.* **32**, 3330-3332, (2007).

14. C.P. Hauri, W. Kornelis, F.W. Helbing, A. Heinrich, A. Couairon, A. Mysyrowicz, J. Biegert, and U. Keller. Generation of intense, carrier-envelope phase-locked few-cycle laser pulses through filamentation. *Appl. Phys. B*, **79**, 673-677, (2004).
15. A. Couairon, J. Biegert, C.P. Hauri, W. Kornelis, F.W. Helbing, U. Keller, and A. Mysyrowicz. Self-compression of ultra-short laser pulses down to one optical cycle by filamentation. *J. Mod. Opt.* **53**, 75-85, (2006).
16. A. Couairon, M. Franco, A. Mysyrowicz, J. Biegert, and U. Keller. Pulse self-compression to the single-cycle limit by filamentation in a gas with a pressure gradient. *Opt. Lett.* **30**, 2657-2659, (2005).
17. C.P. Hauri, A. Guandalini, P. Eckle, W. Kornelis, J. Biegert, and U. Keller. Generation of intense few-cycle laser pulses through filamentation-parameter dependence. *Opt. Express* **13**, 7541-7547, (2005).
18. P. Bejot, J. Kasparian, E. Salmon, R. Ackermann, and J. P. Wolf. Spectral correlation and noise reduction in laser filaments. *Appl. Phys. B* **87**, 1-4, (2007).
19. J. Scharz, P. Rambo, and J.-C. Diels. Ultraviolet filamentation in air. *Optics Communication* **180**, 383-390, (2000).
20. P. Béjot, C. Bonnet, V. Boutou, and J.-P. Wolf. Laser noise compression by filamentation at 400 nm in argon. *Opt. Express* **15**, 13295-13309, (2007).
21. E. Matsubara, K. Yamane, T. Sekikawa, and M. Yamashita. Generation of 2.6 fs optical pulses using induced-phase modulation in a gas-filled hollow fiber. *J. Opt. Soc. Am. B* **24**, 985-989, (2007).
22. H. Wille, M. Rodriguez, J. Kasparian, D. Mondelain, J. Yu, A. Mysyrowicz, R. Sauerbrey, J. P. Wolf, and L. Woste. Teramobile: A mobile femtosecond-terawatt laser and detection system. *Eur. Phys. J.: Appl. Phys.* **20**, 183-190, (2002).
23. S. Skupin, L. Bergé, U. Peschel, F. Lederer, G. Mejean, J. Yu, J. Kasparian, E. Salmon, J. P. Wolf, M. Rodriguez, L. Woste, R. Bourayou, and R. Sauerbrey. Filamentation of femtosecond light pulses in the air: Turbulent cells versus long-range clusters. *Phys. Rev. E* **70**, 046602, (2004).
24. G. Fibich and B. Ilan. Self-focusing of elliptic beams: an example of the failure of the aberrationless approximation. *J. Opt. Soc. Am. B* **17**, 1749-1758, (2000).
25. D. Walter, S. Eyring, J. Lobhreiher, R. Spitzenpfel, and C. Spielmann. Spatial optimization of filaments. *Appl. Phys. B*, **88**, 175-178, (2007).
26. R. Ackermann, E. Salmon, N. Lascoux, J. Kasparian, P. Rohwetter, K. Stelmaszczyk, S. H. Li, A. Lindinger, L. Woste, P. Bejot, L. Bonacina, and J. P. Wolf. Optimal control of filamentation in air. *Appl. Phys. Lett.* **89**, 171117, (2006).
27. M. Kolesik, D.E. Roskey, and Moloney J.V. Conditional femtosecond pulse collapse for white-light and plasma delivery to a controlled distance. *Opt. Lett.* **32**, 2753-2755, (2007).
28. N. Karasawa, R. Morita, H. Shigekawa, and M. Yamashita. Generation of intense ultrabroadband optical pulses by induced phase modulation in an argon-filled single-mode hollow waveguide. *Opt. Lett.* **25**, 183-185, (2000).
29. Z. Zeng, Y. Cheng, X. Song, R. Li, and Z. Xu. Generation of an extreme ultraviolet supercontinuum in a two-color laser field. *Phys. Rev. Lett.* **98**, 203901, (2007).
30. S. Zamith, Y. Ni, A. Gurtler, L.D. Noordam, H.G Muller, and M.J.J Vrakking. Control of atomic ionization by two-color few-cycle pulses. *Opt. Lett.* **29**, 2303-2305, (2004).
31. C.M. Kim, I.J. Kim, and C.H. Nam. Generation of a strong attosecond pulse train with an orthogonally polarized two-color laser field. *Phys. Rev. A* **72**, 033817, (2005).
32. Y. Oishi, M. Kaku, A. Suda, F. Kannari, and K. Midorikawa. Generation of extreme ultraviolet continuum radiation driven by a sub-10-fs two-color field. *Opt. Express* **14**, 7230-7237, (2006).
33. W.G. Wagner, H.A. Haus, and J.H. Marburger. Large-scale self-trapping of optical beams in the paraxial ray approximation. *Phys. Rev.* **175**, 256-266, (1968).
34. NIST Atomic Spectra Database [http://physics.nist.gov/PhysRefData/ASD/lines\\_form.html](http://physics.nist.gov/PhysRefData/ASD/lines_form.html)
35. M. Kolesik and J.V. Moloney. Nonlinear optical pulse propagation simulation: From maxwell's to unidirectional equations. *Phys. Rev. E* **70**, 036604, (2004).
36. M. Kolesik, E.M. Wright, A. Becker, and J.V. Moloney. Simulation of third-harmonic and supercontinuum generation for femtosecond pulses in air. *Appl. Phys. B*, **85**, 531-538, (2006).
37. H. Ehrhardt, Kh. Hesselba, K. Jung, E. Schubert, and K. Willmann. Electron-impact ionization of argon - measurements of triple differential cross-sections. *J. Phys. B* **7**, 69-78, (1974).
38. E.R. Peck and D.J. Fischer. Dispersion of argon. *J. Opt. Soc. Am.* **54**, 1362-1364, (1964).
39. V. Mizrahi and D.P. Shelton. Dispersion of nonlinear susceptibilities of Ar,  $N_2$ , and  $O_2$  measured and compared. *Phys. Rev. Lett.* **55**, 696-699, (1985).
40. M. Mlejnek, E. M. Wright, and J. V. Moloney. Femtosecond pulse propagation in argon: A pressure dependence study. *Phys. Rev. E* **58**, 4903-4910, (1998).
41. Y.P Raizer. Plasma physics. Springer, Berlin Plasma Physics, (1994).
42. A. Couairon, S. Tzortzakis, L. Bergé, M. Franco, B. Prade, and A. Mysyrowicz. Infrared femtosecond light filaments in air: simulations and experiments. *J. Opt. Soc. Am. B* **19**, 1117-1131, (2002).
43. W.H. Press, B.P. Flannery, S.A. Teukolsky, and W.T. Vetterling. Numerical recipes. Cambridge University Press, Cambridge Numerical Recipes, (1989).
44. A. Chiron, B. Lamouroux, R. Lange, J. F. Ripoche, M. Franco, B. Prade, G. Bonnaud, G. Riazuelo, and A. Mysy-

- rowicz. Numerical simulations of the nonlinear propagation of femtosecond optical pulses in gases. *European Physical Journal D* **6**, 383-396, (1999).
45. M. Rodriguez, R. Sauerbrey, H. Wille, L. Woste, T. Fujii, Y. B. Andre, A. Mysyrowicz, L. Klingbeil, K. Rethmeier, W. Kalkner, J. Kasparian, E. Salmon, J. Yu, and J. P. Wolf. Triggering and guiding megavolt discharges by use of laser-induced ionized filaments. *Opt. Lett.* **27**, 772-774, (2002).
  46. J. Kasparian, R. Ackermann, Y.-B. Andre, G. Méchain, G. Mejean, B. Prade, P. Rohwetter, E. Salmon, K. Stelmaszczyk, J. Yu, A. Mysyrowicz, R. Sauerbrey, L. Woste, and J.-P. Wolf. Electric events synchronized with laser filaments in thunderclouds. *Opt. Express* **16**, 5757-5763, (2008).
  47. S. Tzortzakis, G. Méchain, G. Patalano, M. Franco, B. Prade, and A. Mysyrowicz. Concatenation of plasma filaments created in air by femtosecond infrared laser pulses. *Appl. Phys. B* **76**, 609-612, (2003).
  48. W. Liu, F. Gravel, J. F. Theberge, A. Becker, and S.L. Chin. Background reservoir: its crucial role for long-distance propagation of femtosecond laser pulses in air. *Appl. Phys. B* **80**, 857-860, (2005).
  49. J.E. Rothenberg. Pulse splitting during self-focusing in normally dispersive media. *Opt. Lett.* **17**, 583-585, (1992).
  50. A Couairon, G. Méchain, S. Tzortzakis, M. Franco, B. Lamouroux, B. Prade, and A. Mysyrowicz. Propagation of twin laser pulses in air and concatenation of plasma strings produced by femtosecond infrared filaments. *Opt. Comm.* **225**, 177-192, (2003).
- 

## 1. Introduction

Strong interest has been recently devoted to few-cycle pulses (FCP) generation for their properties in both the spectral and time domains. In the time domain, their very short duration can be used to generate high harmonics in rare gases, a step to produce XUV attosecond pulses in order to probe, with attosecond time resolution, phenomena [1, 2, 3] such as coherent molecular dynamics or Rydberg orbital motion. In the Fourier reciprocal space, their octave-broad spectrum can be used in spectroscopy [4] or white-light Lidar applications [5].

Filamentation [6, 7, 8], resulting from the dynamic balance between Kerr self-focusing and defocusing on laser-induced plasma, is now recognized as an efficient way to produce such ultrashort pulses [9, 10, 11, 12, 13, 14, 15, 16, 17]. Moreover, filament-based experiments do not need fine alignment as is the case of capillary-based setups.

Up to now, both experimental and theoretical investigations have focused on filamentation in the infrared (800 nm) and ultraviolet (248 nm) regions [6, 7, 8, 15, 18, 19]. However, recent results showed that filamentation of 400 nm pulses in Argon can also produce a very broad spectrum [20]. Unfortunately, filamentation at 400 nm yields a limited energy on the wings of the continuum induced by self-phase modulation (SPM) [21], which restricts the theoretical minimum pulse duration achievable by this method.

A great deal of effort has been devoted to the control of the plasma channel and the white-light generated during filamentation [8]. Chirp [22], energy, beam size and shape [23], ellipticity [24], spectral and spatial shaping [25, 26] have been investigated. Recently, another way to control filamentation has been proposed theoretically: the two-color filamentation, or *conditional femtosecond pulse collapse* [27] for white-light and plasma delivery to a controlled distance. Launching 600 nm and 800 nm pulses with an adequate time-delay, and a power just below the critical power allows, with the help of air dispersion, to control the location of the filamentation onset.

Such two-color dual filamentation approach could also overcome the limited energy on the wings of the white-light continuum. By combining two pulses with different central wavelength (e.g. 800 nm and 400 nm) in a gas-filled hollow core fiber, the interplay of both XPM and SPM results in a broader spectrum than SPM alone [21, 28]. Two-color filamentation was also used to generate ultrashort deep-ultraviolet (200 nm and 266 nm) [9] or mid-infrared pulses [13] by four-wave mixing (FWM). These processes are very efficient because both pulses are clamped to intensities as high as  $5 \cdot 10^{13} \text{ W.cm}^{-2}$  over several Rayleigh lengths. Moreover, the use of two single-cycle pulses, at frequencies  $\omega$  and  $2\omega$  can enhance the generation of high harmonics, as compared to a single pulse [1, 29, 30, 31, 32]. Simultaneously generating single-cycle pulses

at both 800 nm and 400 nm is therefore particularly promising for attosecond and high-field physics.

In this paper, we study both experimentally and theoretically two-color (800 nm and 400 nm) filamentation in Argon. We show that an adequate time-delay results in co-filamentation of the two pulses, yielding a single, strongly broadened spectrum and opening the way to the simultaneous generation of 400 nm and 800 nm FCP. Moreover, the two-color co-filamentation generates a much longer connected plasma channel than that generated by each of the filaments individually, which could be useful to trigger and control high voltage discharges.

## 2. Materials and methods

### 2.1. Experimental setup

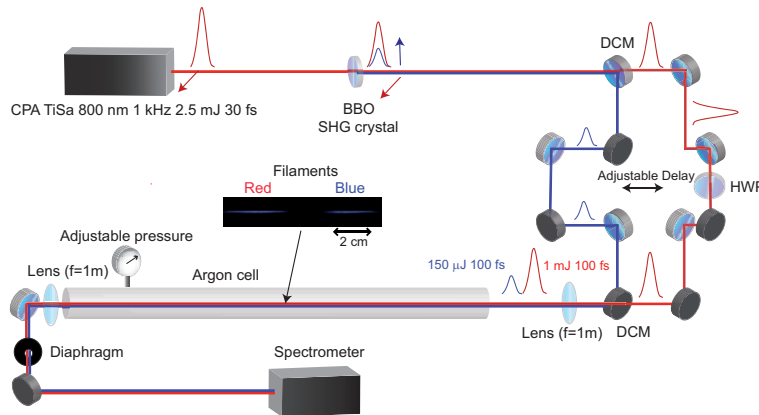


Fig. 1. Experimental setup. **DCM**: Dichroic mirror. **HWP**: Half-waveplate.

The experimental setup is shown in Fig. 1. A Ti:Sa amplifier system (Hidra, Coherent Inc.), delivers 2.5 mJ (stability: 0.5 % rms), 800 nm pulses at a 1 kHz repetition rate. The seed pulse is shaped by a Dazzler in order to shorten the output pulse down to 30 fs. The beam is frequency-doubled to 400 nm using a 0.5 mm thick BBO crystal, providing a typical output energy of 150 – 300 μJ. The remaining NIR (labeled as beam "R", about 1 mJ) and the blue ("B") pulses are separated by a dichroic mirror (DCM). The R polarization is rotated by a zero-order waveplate (WP) and its delay relative to B is adjusted by a delay line, after which the two beams are recombined with another DCM (DCM2). Then, the two collinear beams are focused by a  $f = 1$  m lens in a 2 m long cell filled with 2 bar Argon. We determined the zero-delay between both pulses by optimizing the sum-frequency generation at 266 nm in a 200 μm thick BBO crystal. When either of the two pulses propagates into the cell, a single plasma channel of 2.5 cm length is generated. Such short channel may stem from the moderate initial beam quality, in both the temporal and spatial dimensions. However, as in particular numerical simulations below will show, the actual filaments are longer than the 2.5 cm-long section where the electron density is sufficient to be observed visually, up to beyond 10 cm. As expected from the Marburger formula [33] considering the lens longitudinal chromatic aberration, the B and R filaments start at  $z_B = 90$  cm and  $z_R = 97$  cm, respectively,  $z$  being the propagation distance. The two beams are then collimated at the cell exit by a  $f = 1$  m lens. The core (4 mm in diameter) of the beams are redirected to a spectrometer (Ocean Optics, HR4000, 0.5 nm resolution). Besides, the plasma channels are characterized by side images recorded with a

RGB color-frame digital camera (Nikon D80), with a resolution of about  $30 \mu\text{m}$ . The signal was averaged over 3 s, corresponding to 3000 laser pulses. We checked that the collected light was unpolarized and shows no axial dependence, which excludes both Rayleigh scattering and third-order susceptibility processes, and warrants that only the plasma fluorescence is recorded. To avoid scattered light from either the **R** or the **B** filaments, we considered the green layer ( $450 - 600 \text{ nm}$ ) of the RGB pictures, where several fluorescence emission lines of nitrogen are present, although the main fluorescence signal is in the  $650 - 950 \text{ nm}$  range [34].

## 2.2. Numerical methods

The high intensity within the filaments, as well as their reduced transverse dimension ( $\simeq 100 \mu\text{m}$ ) prevent in-situ measurements. To get insight into the highly non-linear co-filamentation process beyond the experimentally available data, we developed a numerical model aimed at reproducing the actual experimental conditions as closely as possible.

More precisely, we consider two collinearly polarized incident electric fields at  $\lambda_b = 400 \text{ nm}$  and  $\lambda_r = 800 \text{ nm}$  with cylindrical symmetry around the propagation axis  $z$ . They write  $\Re\{\varepsilon_i \exp[i(k_i z - \omega_i t)]\}$ , where  $k_i = \frac{2\pi n_i}{\lambda_i}$  and  $\omega_i = \frac{2\pi c}{\lambda_i}$  ( $i = \mathbf{R}, \mathbf{B}$ ) are the carrier wave number and the frequency, in the slowly varying envelope approximation [35]. This separation of the **R** and **B** radiations is acceptable as long as their spectra do not overlap [36]. Each field is propagated within a classical non-linear Schrödinger equation (NLSE) [7], while their interaction occurs through cross-phase modulation (XPM). We therefore, neglect all phenomena such as  $2\omega_b \pm \omega_r$ ,  $2\omega_r \pm \omega_b$ , as well as higher order processes. The two scalar envelopes evolve according to the coupled propagation equations (1-2):

$$\partial_z \varepsilon_{\mathbf{B}} = \frac{i}{2k_{\mathbf{B}}} \Delta_{\perp}^2 \varepsilon_{\mathbf{B}} - i \frac{k_{\mathbf{B}}''}{2} \partial_t^2 \varepsilon_{\mathbf{B}} - i \Delta_{\perp} \partial_t \varepsilon_{\mathbf{B}} + \frac{ik_{\mathbf{B}}}{n_{\mathbf{B}}} \left( n_{2\mathbf{B}} |\varepsilon_{\mathbf{B}}|^2 + n_{\text{cross}} |\varepsilon_{\mathbf{R}}|^2 \right) \varepsilon_{\mathbf{B}} \quad (1)$$

$$\begin{aligned} & - \frac{ik_{\mathbf{B}}}{2n_{\mathbf{B}}^2 \rho_{c\mathbf{B}}} \rho \varepsilon_{\mathbf{B}} - \frac{1}{2} \sigma_0 \rho \varepsilon_{\mathbf{B}} - \frac{\beta_{\mathbf{B}}^{K_{\mathbf{B}}}}{2} |\varepsilon_{\mathbf{B}}|^{2K_{\mathbf{B}}-2} \varepsilon_{\mathbf{B}} \\ \partial_z \varepsilon_{\mathbf{R}} = & \frac{i}{2k_{\mathbf{R}}} \Delta_{\perp}^2 \varepsilon_{\mathbf{R}} - i \frac{k_{\mathbf{R}}''}{2} \partial_t^2 \varepsilon_{\mathbf{R}} + \frac{ik_{\mathbf{R}}}{n_{\mathbf{R}}} \left( n_{2\mathbf{R}} |\varepsilon_{\mathbf{R}}|^2 + n_{\text{cross}} |\varepsilon_{\mathbf{B}}|^2 \right) \varepsilon_{\mathbf{R}} \quad (2) \\ & - \frac{ik_{\mathbf{R}}}{2n_{\mathbf{R}}^2 \rho_{c\mathbf{R}}} \rho \varepsilon_{\mathbf{R}} - \frac{1}{2} \sigma_{\mathbf{R}} \rho \varepsilon_{\mathbf{R}} - \frac{\beta_{\mathbf{R}}^{K_{\mathbf{R}}}}{2} |\varepsilon_{\mathbf{R}}|^{2K_{\mathbf{R}}-2} \varepsilon_{\mathbf{R}} \end{aligned}$$

where  $t$  refers to the retarded time in the reference frame of the  $800 \text{ nm}$  pulse  $t \rightarrow t - \frac{z}{v_{g\mathbf{R}}}$  with  $v_{g\mathbf{R}} = \frac{\partial \omega}{\partial k} |_{\omega_{\mathbf{R}}}$  corresponding to the group velocity of the  $800 \text{ nm}$  carrier envelope. The terms on the right-hand side of Eq. 1 account for spatial diffraction, second order dispersion, temporal walkoff due to the group-velocity dispersion of the two envelopes, instantaneous self and cross Kerr effects, plasma defocusing and absorption, respectively (Table 1). The Kerr response of Argon is assumed to be instantaneous [6]. In (1),  $\Delta_{\perp} = \frac{1}{v_{g\mathbf{B}}} - \frac{1}{v_{g\mathbf{R}}}$  is the walkoff constant and  $\rho_{c_i} = \frac{\omega_i m_e \varepsilon_0}{q_e^2}$  corresponds to the critical plasma density above which the plasma becomes opaque. In addition, the constant  $\sigma_i = \frac{k_i e^2}{\omega_i m_e \varepsilon_0} \frac{\tau}{1 + (\omega \tau)^2}$  denotes the cross-section for electron-neutral inverse bremsstrahlung ( $\tau$  is the electron-atom relaxation time) and  $\beta_i^{K_i}$  corresponds to the coefficient of multiphoton absorption,  $K_i$  being the minimal number of photons necessary to ionize Argon. This quantity is calculated as  $K_i = \text{mod}\left(\frac{U}{\hbar \omega_i}\right) + 1$  ( $K_{\mathbf{R}} = 11$  and  $K_{\mathbf{B}} = 6$ ), where  $U$

is the ionization potential of Argon ( $U = 15.76 \text{ eV}$  [37]).  $\beta^{K_i}$  is expressed as  $\beta^{K_i} = K_i \hbar \omega_i \rho_{at} \sigma_{K_i}$  where  $\rho_{at}$  is the Argon density and  $\sigma_{K_i}$  is the multiphoton ionization cross section.

The dynamic of the electric field is coupled with the plasma density  $\rho$  by the multiphoton ionization. Hence, the plasma density  $\rho$  follows the equation:

$$\partial_t \rho = \left( \sum_{l=\mathbf{B},\mathbf{R}} \sigma_{K_l} |\varepsilon_l|^{2K_l} \right) \left( 1 - \frac{\rho}{\rho_{at}} \right) + \frac{1}{U} \sum_{l=\mathbf{B},\mathbf{R}} \sigma_l \rho |\varepsilon_l|^2 - \alpha \rho^2 \quad (3)$$

where  $\alpha$  is the recombination time constant.

Table 1. Physical parameters used in the model ( $p$  accounts for the relative gas pressure:  $p = \frac{P}{1\text{bar}}$ )

	$\lambda_{\mathbf{B}} = 400 \text{ nm}$	$\lambda_{\mathbf{R}} = 800 \text{ nm}$
$k'' \text{ (fs}^2 \cdot \text{cm}^{-1}\text{)}$	0.49 $p$ [38]	0.21 $p$
$n_2 \text{ (m}^2 \text{W}^{-1}\text{)}$	4.9. $p 10^{-23}$ [39]	3.2. $p 10^{-23}$
$n_{\text{cross}} \text{ (m}^2 \text{W}^{-1}\text{)}$	1. $p 10^{-23}$	
$K$	6	11
$\beta^K \text{ (m}^{2K-3} \text{W}^{1-K}\text{)}$	1.95. $p 10^{-88}$	3.32. $p 10^{-176}$
$\sigma^K \text{ (s}^{-1} \text{cm}^{2K} \text{W}^{-K}\text{)}$	2.79. $p 10^{-72}$ [6]	5.06. $p 10^{-140}$
$\sigma(1\text{bar}) \text{ (m}^2\text{)}$	2.53 $10^{-24}$	1.01 $10^{-23}$
$\rho_c \text{ (m}^{-3}\text{)}$	6.4 $10^{27}$	1.74 $10^{27}$
$\alpha \text{ (m}^{-3} \text{s}^{-1}\text{)}$	7 $10^{-13}$ [40]	
$\tau \text{ (s)}$	1.9 $10^{-13} p^{-1}$ [41]	

Table 2. Input parameters used in the model. The different focal length for the 800 nm ( $\mathbf{R}$ ) and 400 nm ( $\mathbf{B}$ ) pulses account for longitudinal chromatic aberration of the focusing length used in the experiments.

	$\lambda_{\mathbf{B}} = 400 \text{ nm}$	$\lambda_{\mathbf{R}} = 800 \text{ nm}$
<i>Energy (mJ)</i>	0.150	1
$\Delta t_{FWHM} \text{ (fs)}$	50	30
$\sigma_r \text{ (mm)}$	6	6
<i>Chirp (fs<sup>2</sup>)</i>	-100	-330
$f \text{ (m)}$	1	1.04
<i>Pressure (bar)</i>	2	

The initial conditions are chosen to match the experimental parameters, as summarized in Table 2. We chose an initial plasma density of  $10^9 \text{ e}^- \cdot \text{cm}^{-3}$  [42]. The input electric field envelopes are modeled in focused geometry by two Gaussian profiles with input power  $P_{in_i}$  as

$$\varepsilon_i(r, t, 0) = \sqrt{\frac{2P_{in_i}}{\pi\sigma_{ri}^2}} \cdot \exp\left(-\frac{r^2}{\sigma_{ri}^2} - \frac{t^2}{\tau_i^2} + i\frac{k_i r^2}{2f_i}\right) \quad (4)$$

where  $\sigma_{ri}$  is the intensity quadratic radius,  $\tau_i = \Delta t_{FWHM} / (\sqrt{2 \ln(2)})$  and  $f_i$  is the focal length of the  $\lambda_i$  pulse. Both the initial delay imposed between the two pulses and the linear chirp of the pulses are set in the frequency space:

$$\varepsilon_{\mathbf{R}}(r, \omega, 0) \rightarrow \varepsilon_{\mathbf{B}}(r, \omega, 0) \cdot \exp(i\omega\Delta_t) \cdot \exp(iC_{\mathbf{B}}^2 \omega^2) \quad (5)$$

$$\varepsilon_{\mathbf{R}}(r, \omega, 0) \rightarrow \varepsilon_{\mathbf{R}}(r, \omega, 0) \cdot \exp(iC_{\mathbf{R}}^2 \omega^2) \quad (6)$$

Here,  $\Delta_t$  represents the time delay between the two pulses,  $C_{\mathbf{B}}$  ( $C_{\mathbf{R}}$ ) is the linear chirp parameter of the initial  $\lambda_{\mathbf{B}}$  ( $\lambda_{\mathbf{R}}$ ) pulse.

The above equations have been integrated with a Fourier Split-Step scheme in which all the linear terms are computed in the Fourier space over a half-step while the nonlinear terms are directly computed in the physical space over a second half-step using a Runge-Kutta procedure. To integrate the linear terms of the equation along the  $z$  axis, *i.e.* diffraction and dispersion, we used a fully implicit scheme [43], more stable than the Euler method [44]. On the other hand, for the plasma Eq. (3), an Euler scheme is sufficiently robust. Adaptive steps were used in both the spatial transverse and longitudinal dimensions. The temporal and spatial resolutions at the filament location were  $0.25$  fs and  $1.5$   $\mu\text{m}$ , respectively. We checked that increasing the 2D grid resolution does not influence the final results.

### 3. Results and discussion

#### 3.1. Spectral bridging by co-filamentation

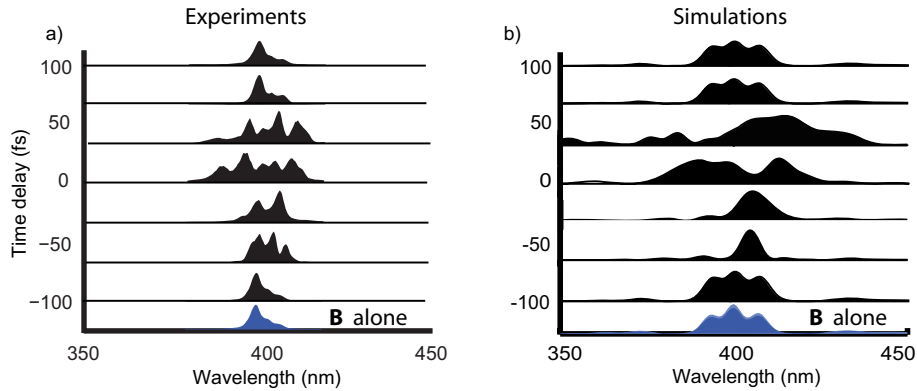


Fig. 2. 400 nm pulse spectrum as function of the relative delay between the pulses centered at 400 nm and 800 nm. The time delay is positive when the NIR pulse (**R**) is launched after the blue one (**B**). The spectrum at the bottom of each series corresponds to the **B** pulse alone. (a) Experimental results, integrated over 4 mm diameter; (b) Numerical simulations. The broader numerical spectrum stems from the consideration of the filament center only, where the broadening is strongest, as well as the non-perfect temporal and spatial profiles of the experimental pulse

When one of the beams propagates independently, spectral broadening is only due to SPM and, to a lesser extent, to the plasma-induced nonlinear phase shift. In the case of dual-color co-filamentation, additional XPM-induced nonlinear phase shift broadens the continuum. Figure 2 displays both the experimental and the theoretical spectrum of the **B** filament output spectrum

as a function of the delay with the **R** pulse. A fine delay tuning allows to control the shape of the blue spectrum output. The numerical results agree qualitatively with the experimental ones, except for the spectral width of the continuum. The simulated spectral broadening critically depends on the delay between the two pulses, as is the case for the experimental data. Comparable delays also yield the same relative broadening. The difference in the absolute spectral width is due to the fact that the experimental data integrate the spectrum over a 4 mm wide region, while the numerical results consider the spectrum in the filament center, where the broadening is strongest. The presence of a pre-pulse in the experiment [17] and an imperfect transverse intensity profile may also contribute to this difference.

The numerical simulations also reproduce well the shape and central wavelength of the **B** spectrum when the delay between both pulses is varied. Launching **R** 50 fs (*i.e.*, a delay comparable with the pulse duration) before (resp. after) **B** enhances the red (resp. blue) part of **B**. This can be qualitatively understood by considering that the instantaneous frequency in a  $\chi^{(3)}$  medium is approximately  $\omega(t) = \omega_0 - \frac{n_2 * \lambda}{c} \frac{\partial I}{\partial t}$  with  $n_2 > 0$  in Argon so that the spectrum is shifted towards the blue (resp. red) in the trailing (resp. leading) edge of the pulse, when  $dI/dt$  is negative (resp. positive). Depending on the sign of the delay, either the leading or trailing part of the considered pulse interacts with the other pulse, resulting in a selective enhancement of the corresponding spectrum side.

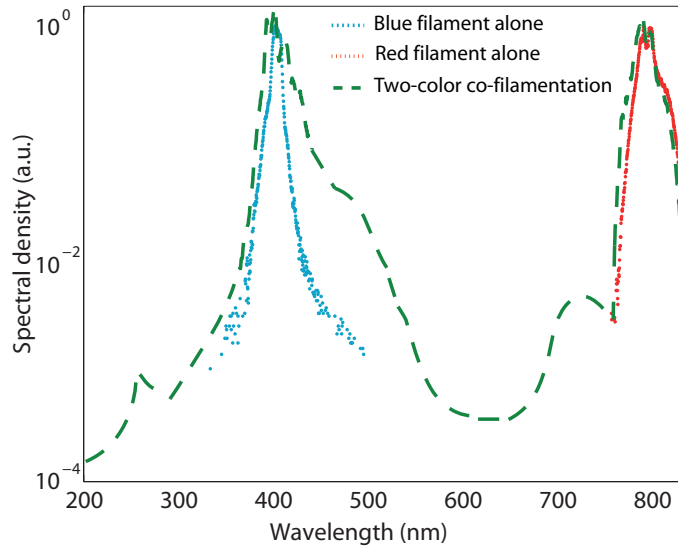


Fig. 3. (a) Experimentally observed influence of co-filamentation on the output spectrum of the supercontinuum. Co-filamentation broadens individual continuum spectra, especially in the blue region, and connects them into a continuum spanning 2 octaves (200 nm - 800 nm). The peak at 266 nm originates from the  $\chi^{(3)}$  mixing  $\frac{1}{266} = \frac{1}{400} + \frac{1}{400} - \frac{1}{800}$

Figure 3 displays the full experimental spectrum of the **B** and **R** pulses, as well as that of the connected continuum generated by the co-propagation of the **B** and **R** with a perfect temporal overlap (0 fs delay). Besides broadening the continuum around the **B** and **R** wavelengths, it also bridges those two continua into a single continuous spectrum spanning over two octaves, which raises the expectation that the corresponding pulses may be as short as 1.4 fs FWHM. Co-propagation also results in a peak at 266 nm, which is not generated by any of the filaments alone (therefore excluding third harmonic generation by the **R** pulse), originating from the  $\chi^{(3)}$

mixing  $\frac{1}{266} = \frac{1}{400} + \frac{1}{400} - \frac{1}{800}$  [9]. This mixing process even enhances the spectral broadening down to at least  $240 \text{ nm}$ , limited by the spectral range of the detection.

### 3.2. Bridging of plasma channels by co-filamentation

When the laser intensity exceeds a few  $10^{12} \text{ W.cm}^{-2}$ , Argon ionizes. The resulting plasma stabilizes the filaments in a dynamic balance with the Kerr effect. Moreover, the plasma decreases the local medium resistivity, which is of high importance to control high-voltage discharges [45] or lightning [46]. Long, highly conductive plasma "wires" are therefore highly desirable in order to increase the triggering and guiding efficiency of the filaments.

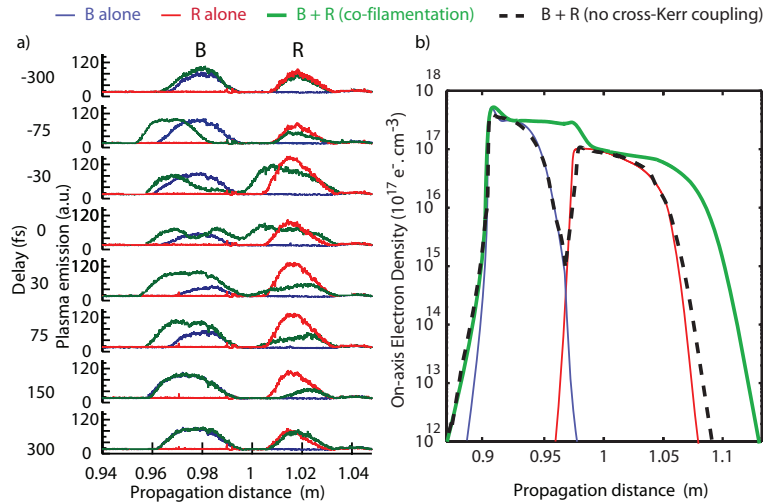


Fig. 4. a) Experimental plasma channel length for several delays. For well adjusted delay, the two plasma channel are concatenated and form a longer plasma channel without any non-ionized region. Blue: **B** induced plasma channel. Red: **R** induced plasma channel. b) Theoretical on-axis plasma channel density for both individual filaments, co-propagating filaments, and collinear filaments without cross-Kerr coupling.

Figure 4(a) depicts the qualitative profile of the electron density as a function of the propagation distance, for several delays between the **R** and **B** filaments. As long as the pulses do not temporally overlap, the resulting plasma density is the sum of the contributions of the two pulses propagating individually, with two  $2.5 \text{ cm}$  long plasma channels, separated by a  $2 \text{ cm}$  long non-ionized (therefore, isolating) region. When the pulses overlap, the two plasma columns do not only connect, but the gap between them is filled by a continuous plasma channel. In other words, co-filamentation bridges the individual plasma channels into a  $9 \text{ cm}$  long channel, corresponding to a 3.6-fold increase of the length as compared with the individual filaments. It is indeed remarkable that this bridging is obtained by the addition of the **B**, which accounts for only 13 % of the overall energy involved in the experiment. The same lever effect is observed in the numerical simulations (Fig. 4(b)). It results in a decrease of the filament resistivity between  $z_1 = 0.9 \text{ m}$  and  $z_2 = 1.07 \text{ m}$ , which is proportional to  $\int_{z_1}^{z_2} 1/\rho(z) dz$ : The co-filamentation reduces this resistivity by a factor 6, as compared to the independent propagation of the individual pulses, *i.e.* when they do not temporally overlap. Such situation contrasts with the concatenation of two plasma channels generated by two collinear  $800 \text{ nm}$  pulses of similar  $4 \text{ mJ}$  pulse energy [47]. In the latter case, an electrical connection is achieved between two filaments, but the end of the first filament is located very close to the onset of the second one.

The resulting doubling of the electrically connected plasma channel length therefore appears as a straightforward effect of the double available energy, rather than of a non-linear interaction between two co-filamenting pulses.

Partial temporal overlap results in intermediate results. The addition of **R** behaves as a supplementary energy reservoir [48] and yields an additional cross-Kerr focusing which shifts the onset of the **B** filaments toward the laser source. Reciprocally, **B** contributes to focusing **R**, but its plasma also defocuses and absorbs **R**. The outcome of these opposite effects depends on the sign of the delay between the pulses. If **R** is launched after **B**, the plasma left behind by **B** tends to defocus the **R** pulse, so that the **R** filament starts later and has a lower plasma density. On the opposite, if **R** is launched before **B**, the cross-Kerr focusing dominates. The resulting plasma channel is more intense and shifts upstream. Therefore, the plasma channel length, density and location can be controlled by adjusting the time delay between the two pulses.

To further demonstrate the contribution of the non-linear coupling between the co-filamenting pulses, we performed the same experiment with two pulses of orthogonal polarization. Such configuration resulted in a much weaker coupling than between pulses with parallel polarization. This weaker coupling stems from the fact that the non-diagonal terms of the third-order susceptibility  $\chi^{(3)}$  tensor amount to one third of the value of the diagonal ones. As a consequence, co-filamentation is much less efficient for pulses of orthogonal polarization, in contrast to the concatenation of plasma channels generated by two collinear 800 nm pulses [47], which is independent from the relative polarization of the two pulses [50]. The key role of non-linear coupling between the co-filamenting pulses is also demonstrated by the fact that the numerical simulations do not need to include two-color multiphoton ionization to reproduce the experimentally observed bridging of the plasma channels. On the other hand, setting the non-linear interaction term to zero in the simulations leads to the disappearance of the bridging (see dotted line in Fig. 4(b)).

The need for a non-linear coupling between the two co-filamenting pulses sets the upper limit to the non-ionized gaps that may be bridged by co-filamentation. Such coupling requires a simultaneous high intensity of both the **R** and **B** pulses, colocated in the non-ionized gap region. Therefore, gaps much longer than the length of the individual filaments will not be able to be bridged by co-filamentation.

### 3.3. Spatio-temporal dynamics of copropagation

To get a better insight on the physics of co-filamentation, we simulated the temporal and transverse intensity mappings, which exhibit rich spatio-temporal deformations in the course of this dual-color process. Figs. 5 and 6 display the **R** (resp. **B**) calculated intensity as a function of time and radial location, for several propagation distances. In both figures, the first column corresponds to the filamentation of a single color pulse, while the second shows the result of the co-filamentation process. The initial delay between the two pulses is set to 10 fs (*i.e.*, the **B** precedes the **R** pulse by 10 fs). These simulations show in particular that the **R** filament diameter is larger than that of **B** (250  $\mu m$  vs. 30  $\mu m$ ), so that the latter is submitted to cross-Kerr effect on a fraction of its cross-section only, while the full **B** filament is influenced by the **R** one. This difference in diameters therefore explains why **R** is more affected than **B** by co-filamentation, from the points of view of both the continuum spectrum and the plasma channels length and position.

The mechanism of co-filament-assisted spectral broadening of **B** is also well illustrated by the simulations. When the **B** intensity reaches the multiphoton ionization threshold, the **R** pulse core is both absorbed by multiphoton absorption and diffracted by the plasma. The cross-Kerr lens generated by the blue filament shifts the **R** focus upstream. Then ( $z = 96$  cm), if **R** is not present, **B** filament intensity decreases because of both plasma absorption and group-velocity

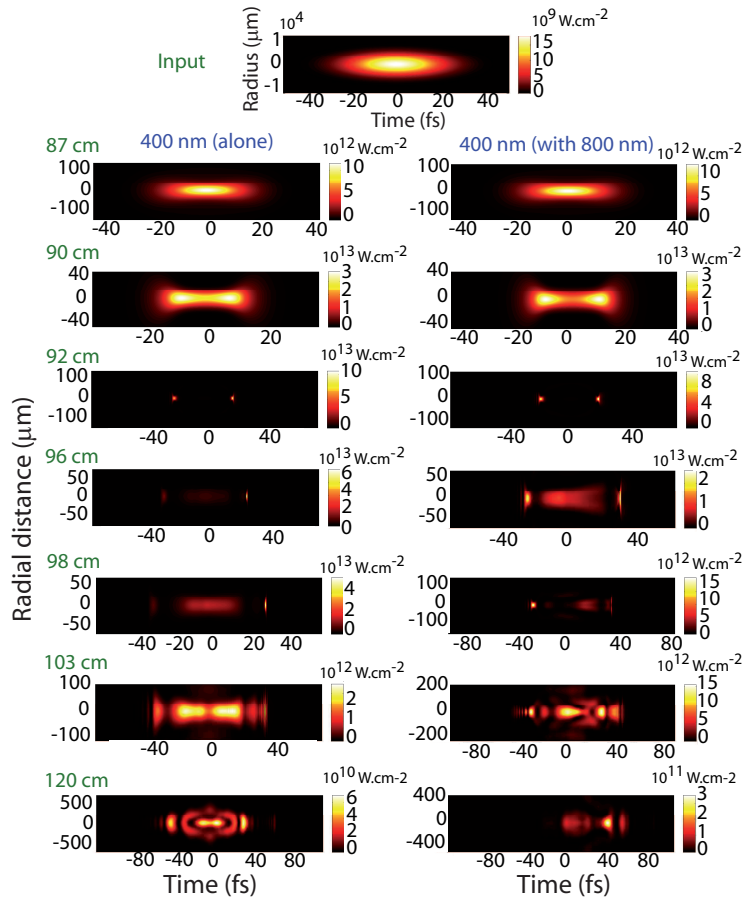


Fig. 5. One- or two-color filamentation dynamic for the 400 nm (**B**) pulse. Left: **B** intensity for several distances when propagating alone. Right: **B** intensity for the same distances when the **R** filament copropagates

dispersion. **B** then splits in the time domain [49] and its spectrum significantly broadens. Conversely, if the **R** pulse is present, the spiky blue pulse experiences more nonlinear phase shift due to the combined effects of XPM and the plasma blue shift, which broadens the spectrum. The shape of the resulting continuum depends on the delay between the two pulses and determines which of the spikes in the **B** pulse experiences the **R**-induced phase shift.

As could be expected from the width of the spectrum corresponding to the co-propagating pulses (Fig. 3), co-filamentation even leads to the formation of almost FCP (about 10 fs FWHM for both pulses, see Figs. 5 and 6 at  $z = 120$  cm) without requiring the pulse post-processing which is usually needed when generating FCP by filamentation [14]. Moreover, in view of attosecond pulse generation, the simultaneous availability of both **R** and **B** FCP could help the generation of such XUV pulses.

Further optimization of the co-filamentation may be obtained in the future by investigating the effect of the gas type and pressure. Also, atmospheric applications can reasonably be envisioned since the filamentation conditions in Argon are, to the first order, comparable to those of air, and the pressure investigated in the present work, namely 2 bars, is of the same order of

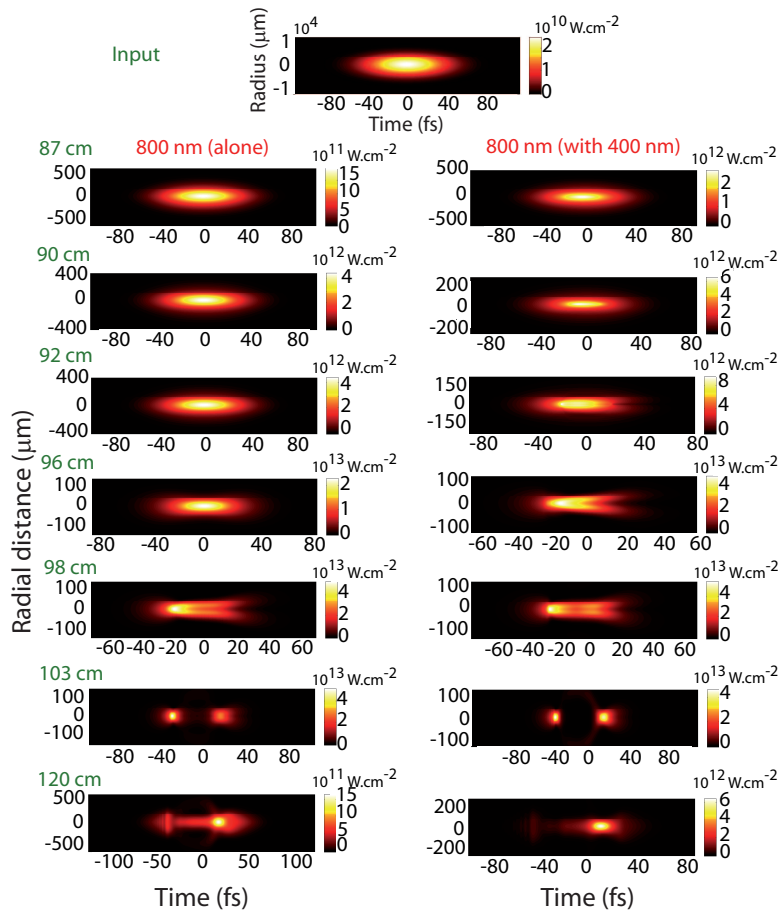


Fig. 6. One- or two-color filamentation dynamic for the **R** pulse. Left: **R** intensity for several distances when propagating alone. Right: **R** intensity for the same distances when the **B** filament copropagates

magnitude as the atmospheric pressure. However, if considering long-distance propagation and high-energy beams, the influence of the modulational instability of already multifilamenting beam onto the interaction between the two pulses will have to be investigated. The corresponding expectedly very rich physics is however beyond the scope of the present paper.

#### 4. Conclusion

We investigated both experimentally and theoretically the two-color co-filamentation of ultrashort laser pulses at 400 nm (**B**) and 800 nm (**R**). Temporally overlapping the two pulses bridges their two filaments. It results in both a spectacular enhancement of the spectral broadening over two octaves, and a connected plasma more than 3 times longer than the initial ones. Moreover, the generation of twin almost-few-cycle pulses at both **B** and **R** could provide an elegant way to produce attosecond pulses generation without any post-processing such as chirp compensation or phase shaping. The pulses with extremely broad spectra could also be used for the coherent control of states spanning over a large energy interval[4]. The extended plasma channel length could also be useful for the control of high-voltage discharges and lightning [46].

## **Acknowledgments**

This work was supported by the Swiss NSF (contracts 200021-111688 and 200021-116198), and the Swiss SER in the framework of COST P18 (Action C06.0114), as well as the Boninchi and Schmideiny foundations. We gratefully acknowledge L. Bonacina for very fruitful discussions. We also thank M. Moret for his computational support.